



Stress induced birefringence in hybrid TIR/PBG guiding solid photonic crystal fibers

Lyngsøe, Jens Kristian; Mangan, Brian Joseph; Olausson, Christina Bjarnal Thulin; Roberts, John

Published in:
Optics Express

Link to article, DOI:
[10.1364/OE.18.014031](https://doi.org/10.1364/OE.18.014031)

Publication date:
2010

Document Version
Publisher's PDF, also known as Version of record

[Link back to DTU Orbit](#)

Citation (APA):
Lyngsøe, J. K., Mangan, B. J., Olausson, C. B. T., & Roberts, J. (2010). Stress induced birefringence in hybrid TIR/PBG guiding solid photonic crystal fibers. *Optics Express*, 18(13), 14031-14040.
<https://doi.org/10.1364/OE.18.014031>

General rights

Copyright and moral rights for the publications made accessible in the public portal are retained by the authors and/or other copyright owners and it is a condition of accessing publications that users recognise and abide by the legal requirements associated with these rights.

- Users may download and print one copy of any publication from the public portal for the purpose of private study or research.
- You may not further distribute the material or use it for any profit-making activity or commercial gain
- You may freely distribute the URL identifying the publication in the public portal

If you believe that this document breaches copyright please contact us providing details, and we will remove access to the work immediately and investigate your claim.

Stress induced birefringence in hybrid TIR/PBG guiding solid photonic crystal fibers

J. K. Lyngsø,^{1,2*} B. J. Mangan,¹ C. B. Olausson^{1,2}
and P. J. Roberts²

¹NKT Photonics A/S, Blokken 84, DK-3460 Birkerød, Denmark

²DTU Fotonik, Technical University of Denmark, Ørstedes Plads 343, DK-2800 Kgs. Lyngby, Denmark

*jkl@nktphotonics.com

Abstract: We report on two types of polarization maintaining solid photonic crystal fibers that guide light by a combination of a photonic bandgap and total internal reflection. Group and phase birefringence are studied experimentally and numerically for stress-applying parts made from B-doped and F-doped silica. The stress field originating from Ge-doped cladding rods is shown to interfere with the stress field from the B-doped and F-doped rods. Since the differential expansion coefficients of B-doped and F-doped silica have opposite signs this interference is either destructive or constructive. Consequently, we found that the fiber with F-doped stress applying parts has the highest modal phase birefringence, and polarization cross talk is characterized by an h-parameter below $3 \cdot 10^{-5} \text{ m}^{-1}$.

©2010 Optical Society of America

OCIS codes: (060.2420) Fibers, polarization-maintaining; (060.4005) Microstructured fibers.

References and links

1. A. Isomäki, and O. G. Okhotnikov, "All-fiber ytterbium soliton mode-locked laser with dispersion control by solid-core photonic bandgap fiber." *Opt. Express* **14**(10), 4368–4373 (2006).
2. S. Ramachandran, "Dispersion-Tailored Few-Mode Fibers: A Versatile Platform for In-Fiber Photonic Devices," *J. Lightwave Technol.* **23**(11), 3426–3443 (2005).
3. S. Ramachandran, S. Ghalmi, J. Nicholson, M. F. Yan, P. Wisk, E. Monberg, and F. V. Dimarcello, "Demonstration of Anomalous Dispersion in a Solid, Silica-Based Fiber at $\lambda < 1300 \text{ nm}$," In *Optical Fiber Communication Conference and Exposition and The National Fiber Optic Engineers Conference*, Technical Digest (CD) p. PDP3 (Optical Society of America, 2006).
4. A. Shirakawa, H. Maruyama, K. Ueda, C. B. Olausson, J. K. Lyngsø, and J. Broeng, "High-power Yb-doped photonic bandgap fiber amplifier at 1150–1200 nm," *Opt. Express* **17**(2), 447–454 (2009).
5. A. Cerqueira S. Jr., F. Luan, C. M. B. Cordeiro, A. K. George, and J. C. Knight, "Hybrid photonic crystal fiber," *Opt. Express* **14**(2), 926–931 (2006).
6. R. Goto, S. D. Jackson, S. Fleming, B. T. Kuhlmeier, B. J. Eggleton, and K. Himeno, "Birefringent all-solid hybrid microstructured fiber," *Opt. Express* **16**(23), 18752–18763 (2008).
7. G. Bouwmans, L. Bigot, Y. Quiquempois, F. Lopez, L. Provino, and M. Douay, "Fabrication and characterization of an all-solid 2D photonic bandgap fiber with a low-loss region ($< 20 \text{ dB/km}$) around 1550 nm," *Opt. Express* **13**(21), 8452–8459 (2005).
8. S. C. Rashleigh, "Measurement of fiber birefringence by wavelength scanning: effect of dispersion," *Opt. Lett.* **8**(6), 336–338 (1983).
9. K. Takada, J. Noda, and R. Ulrich, "Precision measurement of modal birefringence of highly birefringent fibers by periodic lateral force," *Appl. Opt.* **24**(24), 4387–4397 (1985).
10. N. Shibata, M. Tsubokawa, M. Ohashi, K.- Kitayama, and S. Seikai, "Birefringence and polarization mode dispersion in a coil of a single-mode fiber," *J. Opt. Soc. Am. A* **3**(11), 1935–1940 (1986).
11. P. McIsaac, "Symmetry-Induced Modal Characteristics of Uniform Waveguides — I: Summary of Results," *IEEE T. Microw. Theory* **23**(5), 421–429 (1975).
12. T. A. Birks, F. Luan, G. J. Pearce, A. Wang, J. C. Knight, and D. M. Bird, "Bend loss in all-solid bandgap fibres," *Opt. Express* **14**(12), 5688–5698 (2006).
13. G. W. Scherer, "Stress-optical effects in optical waveguides," *J. Non-Cryst. Solids* **38–39**, 201–204 (1980).
14. P. K. Bachmann, W. G. Hermann, H. Wehr, and D. U. Wiechert, "Stress in optical waveguides. 1: Preforms," *Appl. Opt.* **25**(7), 1093–1098 (1986).
15. R. Stolen, "Calculation of stress birefringence in fibers by an infinitesimal element method," *J. Lightwave Technol.* **1**(2), 297–301 (1983).
16. P. Chu, and R. Sammut, "Analytical method for calculation of stresses and material birefringence in polarization-maintaining optical fiber," *J. Lightwave Technol.* **2**(5), 650–662 (1984).

17. K. Tsai, K. Kim, and T. Morse, "General solutions for stress-induced polarization in optical fibers," *J. Lightwave Technol.* **9**(1), 7–17 (1991).
 18. Y. Huang, A. Sarkar, and P. Schultz, "Relationship between composition, density and refractive index for germania silica glasses," *J. Non-Cryst. Solids* **27**(1), 29–37 (1978).
 19. S. Takahashi, and S. Shibata, "Thermal variation of attenuation for optical fibers," *J. Non-Cryst. Solids* **30**(3), 359–370 (1979).
 20. J. Sakai, and T. Kimura, "Birefringence caused by thermal stress in elliptically deformed core optical fibers," *IEEE J. Quantum Electron.* **18**(11), 1899–1909 (1982).
 21. R. Guan, F. Zhu, Z. Gan, D. Huang, and S. Liu, "Stress birefringence analysis of polarization maintaining optical fibers," *Opt. Fiber Technol.* **11**(3), 240–254 (2005).
 22. P. K. Bachmann, W. Hermann, H. Wehr, and D. U. Wiechert, "Stress in optical waveguides. 2: Fibers," *Appl. Opt.* **26**(7), 1175–1182 (1987).
 23. P. K. Bachmann, D. U. Wiechert, and T. P. M. Meeuwse, "Thermal expansion coefficients of doped and undoped silica prepared by means of PCVD," *J. Mater. Sci.* **23**(7), 2584–2588 (1988).
 24. M. Kyoto, Y. Ohoga, S. Ishikawa, and Y. Ishiguro, "Characterization of fluorine-doped silica glasses," *J. Mater. Sci.* **28**(10), 2738–2744 (1993).
-

1. Introduction

Solid photonic bandgap fibers (SPBGF) are useful for intracavity dispersion control in pulsed lasers [1]. For short pulse delivery, however, polarization noise can degrade the output pulse shape and ultimately limit the achievable pulse duration. This can be avoided by making the laser system polarization maintaining. The photonic bandgap cladding allows single mode operation and anomalous dispersion at 1030 nm, while having a relatively large mode field diameter. These properties are not simultaneously achievable using a conventional total internal reflection (TIR) guiding fiber. Higher order mode (HOM) conversion in few moded TIR guiding fibers, via long period gratings, has been demonstrated to take advantage of the anomalous dispersion of higher order modes [2,3]. Polarization maintenance is, however, difficult to implement with this configuration. Even though propagation in a single HOM can be polarization stable, the coupling in and out of the HOM is critical. The bandgap fiber approach, on the other hand, readily enables polarization maintaining operation and also has the benefit of acting as a spectral filter due to the finite bandwidth of the photonic bandgaps [4].

2. Fiber fabrication

The fibers were fabricated using the stack and draw technique. Graded index Ge-doped silica rods, with a maximum refractive index difference of + 2.4% surrounded with a pure silica jacket, were stacked in a hexagonal array making up the microstructured cladding. In the center of the structure one of the Ge-doped rods was replaced with a pure silica rod (Heraeus F300) to form the low index core. To implement stress induced birefringence, two Ge-doped rods near the core were replaced by stress applying parts. Fibers with two different choices for the stress-applying parts (SAPs) were fabricated, one incorporating Boron doped silica and the other with Fluorine doped silica as listed in Table 1. The B and F-doped regions both have a top-hat refractive index profile, at -0.4% and -0.7% relative to the pure silica background, respectively. This means that in the direction of the stress applying parts, the confinement is dominated by TIR, thus the fiber is not a pure bandgap guiding fiber, but rather a hybrid TIR/PBG guiding fiber [5,6].

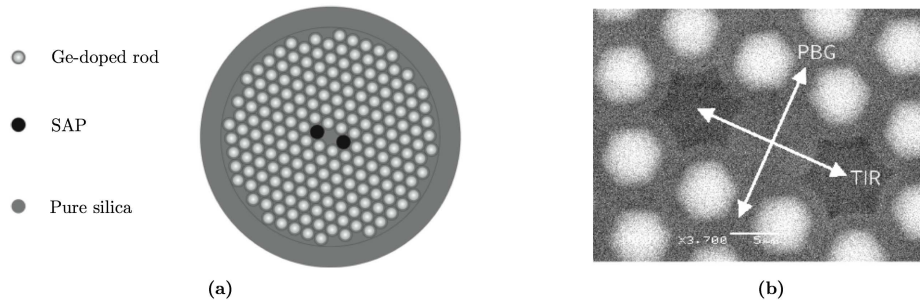


Fig. 1. (a) Schematic drawing of the fiber preform. (b) Scanning electron microscope image of the end face of fiber I.

Figure 1(a) is a diagram of the assembled fiber preform and Fig. 1(b) is a scanning electron microscope image of the end face of fiber I. The lower transition temperature of the borosilicate glass leads to deformation of the stress applying parts as is evident from the SEM.

Table 1. Fabricated fiber properties

Fiber	SAP type	SAP index diff. (%)	Pitch, Λ (μm)
I	B-doped	-0.4	8.6
II	F-doped	-0.7	8.3

3. General properties

The focus is on the 3rd order bandgap, mainly because of the dispersion properties and the relatively small bend sensitivity of this bandgap [7]. Except for polarization maintenance, fibers I and II have very similar optical properties and the current section is primarily based on measurements of fiber I. Even though these fibers guide light by a combination of TIR and photonic bandgap mechanisms, the photonic bandgap properties are conserved. The measured transmission spectrum is shown in Fig. 2(a). It reveals that transmission occurs over a number of separate wavebands, which is indicative of photonic bandgap confinement.

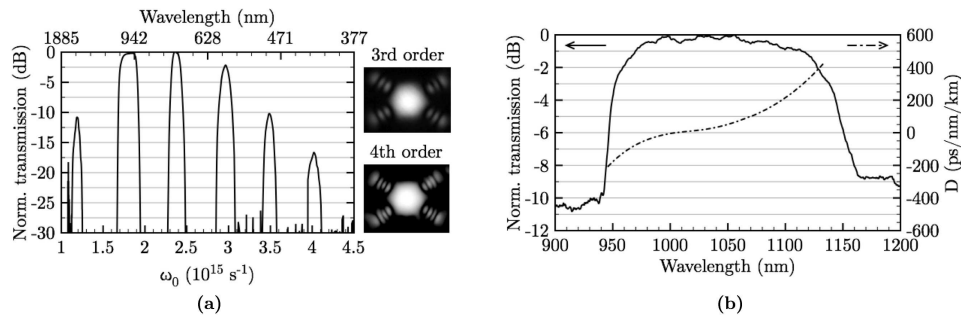


Fig. 2. (a) Transmission measurement on a 3 m section of fiber I. (b) Transmission measurement together with group velocity dispersion of the 3rd order bandgap.

The two insets show near field images of the HE_{11} -like mode profiles in the 3rd and 4th order bandgaps, respectively, where the number of field lobes in the first ring of Ge-doped cladding rods reveal the order of the operating bandgap. The 3rd order bandgap of fiber I, with pitch $\Lambda = 8.6 \mu\text{m}$, is centered at 1050 nm. The group velocity dispersion, shown in Fig. 2(b), is dominated by waveguide dispersion of the PBG confinement. Therefore, as for pure PBG

guiding fibers, the dispersion evolves from normal to anomalous over the bandgap, with the zero dispersion wavelength located at approximately 1000 nm.

Both fibers I and II exhibit a transmission loss between 20 and 30 dB/km over the bandgap, which is comparable to a previously reported pure bandgap guiding structure [7].

4. Polarization maintenance

4.1 Birefringence (Fiber I)

The group birefringence was measured using the scanning wavelength method [8]. Due to the large dispersion in group birefringence over the bandgap, the measurement was repeated with four different lengths of fiber. From the fringe spacing ($\Delta\lambda$), the absolute value of the group birefringence is given by

$$|Bg(\lambda)| = \frac{\lambda^2}{\Delta\lambda L}, \quad (1)$$

where L in Eq. (1) is the fiber length and λ is the wavelength.

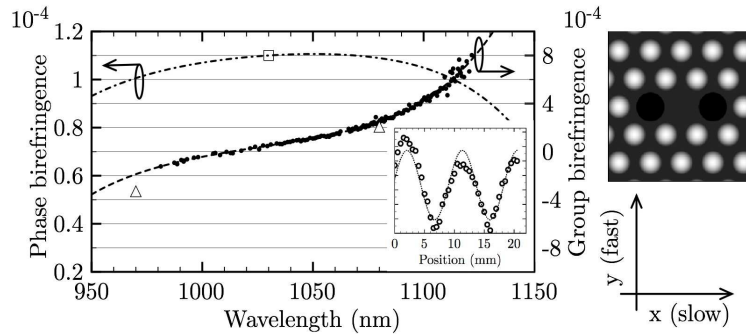


Fig. 3. Measured birefringence of fiber I. Solid circles show the measured group birefringence. The open triangles display the group birefringence calculated from the DGD measurement. The open square is the measured modal phase birefringence calculated from the periodic lateral force measurement displayed in the inset. A representation of the fiber and the adopted coordinate system are also shown.

The resulting group birefringence from all four measurements is plotted in Fig. 3 as solid circles. The modal phase birefringence was measured at 1030 nm using a periodic lateral force approach [9]. The measurement result is shown in the inset of Fig. 3 with a sinusoidal fit. The period of this function corresponds to the modal phase birefringence beat length of the fiber at 1030 nm. This is measured to be $L_B(1030 \text{ nm}) \approx 9.3 \text{ mm}$, leading to a modal phase birefringence $B(1030 \text{ nm}) \approx 1.1 \cdot 10^{-4}$. The wavelength dependence was estimated by extrapolation, using a Taylor expansion to first order:

$$\begin{aligned} B(\lambda + \Delta\lambda) &\approx B(\lambda) + \frac{dB}{d\lambda} \Delta\lambda \\ &= B(\lambda) + \frac{B(\lambda) - Bg(\lambda)}{\lambda} \Delta\lambda. \end{aligned} \quad (2)$$

Where the relation between group and phase birefringence has been used. Hence the modal phase birefringence plotted in Fig. 3 was extrapolated from the value at 1030 nm by fitting a 5th order polynomial to the group birefringence and using Eq. (2) iteratively across the bandgap. The sign of the group birefringence was found by measuring the differential group delay (DGD) at 970 nm and 1080 nm, using a low coherence Mach-Zehnder interferometer in

the time domain. The two DGD measurements are plotted in Fig. 3 as open triangles. The sign of the modal phase and group birefringence corresponds to

$$B = n_{eff}^x - n_{eff}^y \quad (3)$$

$$Bg = n_g^x - n_g^y,$$

where n_g in Eq. (3) is the group index and the fiber axis directions are given by the inset in Fig. 3. As for conventional PANDA fibers, the slow axis is aligned parallel with the SAPs.

4.2 Birefringence (Fiber II)

Figure 4 shows the measured group birefringence of fiber II along with a 5th order polynomial fit. The measurement that determines the phase birefringence beat length to be $L_B(1020 \text{ nm}) \approx 6.6 \text{ mm}$, is displayed in the inset.

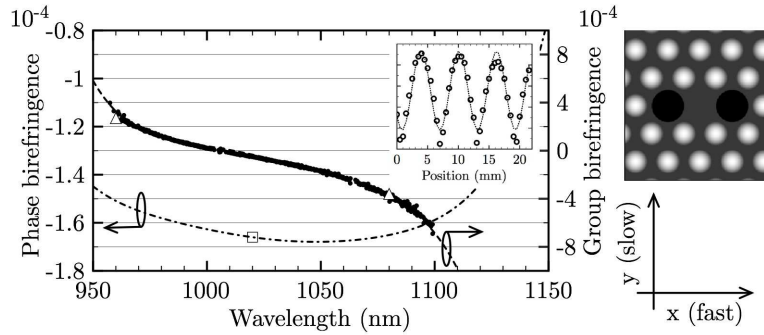


Fig. 4. As in Fig. 3, but for fiber II.

This implies a modal phase birefringence $B(1020 \text{ nm}) \approx 1.66 \cdot 10^{-4}$. The open triangles again give the sign of the group birefringence calculated from differential group delay measurements at 960 nm and 1080 nm. The fast/slow axis alignment is found to be rotated 90° compared to the B-doped fiber. Furthermore, the modal phase birefringence is approximately 1.5 times larger than in fiber I. This behavior is attributed to constructive interference between the stress fields from the cladding rods and the F-doped SAPs, and is examined numerically in section 5.

4.3 Polarization cross talk (Fiber II)

The polarization cross talk (PCT) of fiber II was measured using a conventional crossed polarizer setup, where linear polarized light was launched aligned with one of the principle axis of the fiber. At the fiber output the optical power was measured in each of the principle axes by rotating an analyzer. The h-parameter is a measure of the fraction of optical power coupling from one polarization state to the other per propagation length. The h-parameter was estimated from the polarization cross talk as

$$h = \frac{10^{PCT/10}}{L}, \quad (4)$$

where PCT is on a dB scale and L is the fiber length. PCT was measured on a 100 meter long fiber similar to fiber II, but with a slightly larger pitch.

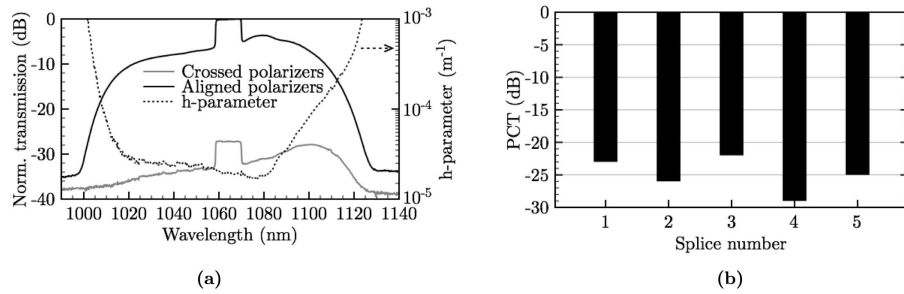


Fig. 5. (a) Measured polarization cross talk. The power difference at 1060 nm was caused by the supercontinuum pump. (b) Measured polarization cross talk at 1060 nm over 90 m. Results are given for five different PM aligned splices to a 1 m pigtail

Figure 5(a) is a plot of the h-parameter calculated from the measured PCT value. Additionally, a one meter long Nufern PM960 XP fiber was PM aligned and spliced to the input end of a 90 m long section of fiber II. A PCT measurement at 1060 nm, including the pigtail, was repeated for five different splices. The results are shown in Fig. 5(b) and the average and minimum PCT were -25 dB and -29 dB, respectively. This corresponds to an h-parameter of $3.5 \cdot 10^{-5}$ and $1.4 \cdot 10^{-5}$. Thus the fiber demonstrates robust polarization maintenance.

5. Numerical modeling

In a fiber where form induced birefringence is negligible, the modal phase and group birefringence can be estimated by treating the stress field as a perturbation. One starts by solving for the mode field distribution of the fiber by considering the material refractive indices as isotropic. Then, by overlapping the distribution of the normalized electric field intensity and the material birefringence caused by the differential stress field, the modal phase birefringence can be calculated [10]:

$$B = C \frac{\iint [\sigma_x(x, y) - \sigma_y(x, y)] |\mathbf{E}(x, y)|^2 dx dy}{\iint |\mathbf{E}(x, y)|^2 dx dy}. \quad (5)$$

Where C is the stress optical coefficient, $|\mathbf{E}(x, y)|^2$ is the HE_{11} -like mode electric field intensity and $[\sigma_x(x, y) - \sigma_y(x, y)]$ is the differential stress field.

5.1 Guided mode field and effective index

The mode field distribution and the related mode effective index were calculated using a finite difference frequency domain method.

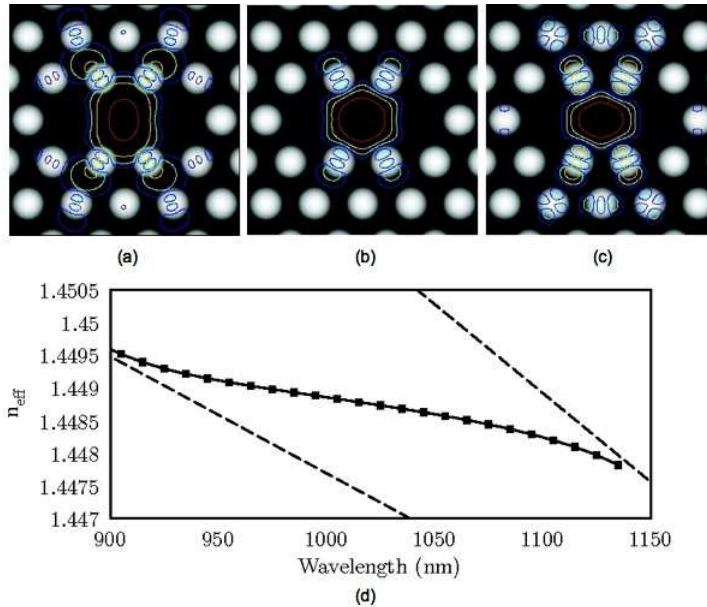


Fig. 6. (a-c) Contour plots of the calculated mode field intensity distributions at the short wavelength edge, center and long wavelength edge of the 3rd order bandgap. (d) Calculated effective index as function of wavelength.

To save calculation time, the computational domain was reduced to a quarter of the fiber cross section, which is the smallest allowed domain when considering a cross section with two fold mirror and rotation symmetry [11]. The quarter domain was set up using 90,000 grid points. The index profile of the Ge-doped cladding rods was found by fitting a quadratic function to the index profile of the graded index Ge-doped preform used. The refractive index of the silica background was set to $n_s = 1.45$ and the cladding pitch was set to $\Lambda = 8.6 \mu\text{m}$ for absolute comparison with the fabricated fibers. The mode field distribution at three different wavelengths, as well as the effective index as a function of wavelength, is shown in Fig. 6. At the short wavelength side of the bandgap (Fig. 6(a)), coupling with the LP_{12} -like cladding mode is evident. Similarly, at the long wavelength side of the bandgap (Fig. 6(c)), coupling with the LP_{21} -like cladding mode occurs [12].

5.2 Differential stress field

In the following discussion, hydrostatic pressure and mechanically induced stress from the fiber drawing process are in general ignored, except for F-doped inclusions, where the mechanically induced stress dominates at the fiber level. Therefore, the basic stress analysis is based on thermal stress caused by a difference in the thermal expansion coefficients (α_i) of the constituent materials.

To accurately calculate the thermal stress field at the fiber level, the complete thermal history of the glass should in principle be taken into account by appropriately integrating Young's modulus ($E_i(T)$), Poisson's ratio ($\nu_i(T)$) and the expansion coefficient ($\alpha_i(T)$) from the setting temperature to room temperature [13]. Here, the simpler approach used in [14] is adopted, where ($E_i(T)$) and $\nu_i(T)$ is approximated to the pure silica values $E = 7830 \text{ kg/mm}^2$ and $\nu = 0.164$, and the thermal expansion coefficient is a thermal average, such that the integration is avoided. The differential stress field of arbitrarily shaped inclusions can be calculated numerically [15]. If the stress applying parts are treated as circular in cross-section, the differential stress field can be found analytically [16,17].

There is in general some dispute in the literature regarding setting temperatures and average expansion coefficients for Ge and B-doped silica. As proposed by Bachmann *et al.*

[14], the setting temperature of Ge-doped silica was taken from [18]. A mole % of 25 corresponds to a setting temperature of $T_{Ge} = -800^{\circ}\text{C}$. The differential expansion coefficient for Ge-doped silica is estimated from [19] to be $\alpha_{Ge} = -1.7 \cdot 10^{-6}$. The values for B-doped silica were estimated from [20,21] to be $T_B = -1000^{\circ}\text{C}$ and $\alpha_B = -1.42 \cdot 10^{-6}$, in correspondence with a mole % of 15. From the average differential expansion coefficients it is obvious that the Ge-doped inclusions contribute significantly to the overall stress field and should be included in the numerical model. Data on F-doped silica is scarce and apparently the expansion coefficient is highly dependent on the thermal history of the material [14]. In the following, a differential thermal expansion coefficient of $\alpha_F = 2 \cdot 10^{-7}$ [23] and setting temperature $T_F = -600^{\circ}\text{C}$ [24] are used, assuming that the setting temperature corresponds to a viscosity of 10^{13} Poise. Thus it is evident that the thermal stress caused by F-doped silica is only moderate. On the other hand, mechanically induced stress from the fiber draw enhances the differential stress caused by F-doped silica. For the current doping level and draw tension (the fibers were drawn with a tension of $\gamma \approx 60 \text{ N/mm}^2$) the enhancement of the stress field has been shown to be approximately 8 times [22]. The fiber draw on the other hand tends to decrease the differential stress caused by Ge-doped silica, but since the thermal induced stress is much larger than for F-doped silica the effect is less significant. If it is assumed that the stress field caused by the F-doped inclusions is enhanced 6 times during the draw and this effect is ignored for B and Ge-doped silica, the calculated birefringence is in good agreement with the observed birefringence over the entire wavelength range of the 3rd order bandgap. Thus in the following the stress field caused by the F-doped inclusions is estimated by multiplying the differential thermal expansion coefficient, α_F by 6.

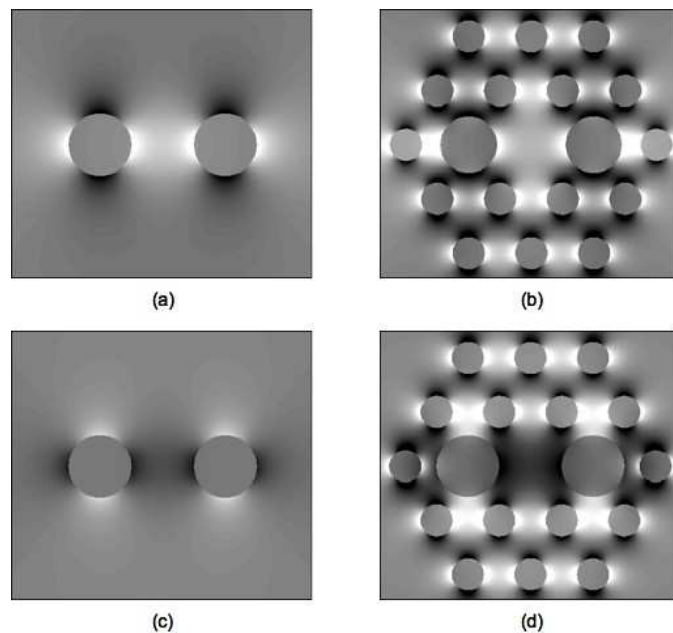


Fig. 7. Differential stress field ($\sigma_x - \sigma_y$) in the core region, where white and black regions correspond to positive and negative differential stress, respectively. (a) B-doped inclusions only, resulting in a positive differential stress field in the fiber center. (b) Full B-doped structure, where the stress field from the Ge-doped rods destructively interferes with the stress field from the B-doped rods. (c) F-doped inclusions only, with a negative differential stress field in the center. (d) Full F-doped structure where the stress field from the Ge-doped rods constructively interferes with the stress field from the F-doped rods.

With regard to the stress contribution, the Ge-doped inclusions were conveniently treated as having a top-hat mole concentration, with a radius scaled such that the total mole

concentration was conserved. This means that the radii of the Ge-doped, the B-doped and the F-doped inclusions used were 0.26, 0.45 and 0.5 Λ , respectively. Only the two first rings of inclusions around the core region were considered as contributing to the stress where the guided mode has significant field intensity.

Figure 7 shows the calculated differential stress fields for the considered structures. Table 2 is a list of the calculated material birefringence at the fiber center (B_0), for each of these structures. Since the Ge and B-doped rods both have negative differential expansion coefficients their stress fields destructively interfere at the fiber center.

Table 2. Various calculated differential stress fields at the fiber center.

Structure	B_0 (10^{-5})
B-doped SAPs only	19
F-doped SAPs only	-12
Fiber I	13
Fiber II	-18

The positive differential expansion coefficient of the F-doped inclusions, on the other hand, leads to constructive interference with the stress fields of the cladding rods. Consequently, the presence of the PBG cladding rods lowers the material birefringence induced by B-doped stress rods, but raises the material birefringence induced by F-doped stress rods.

5.3 Numerically calculated birefringence

Using Eq. (5) with the mode field distributions found in section 5.1 and the differential stress fields found in section 5.2, the modal phase birefringence can be calculated over the bandgap for the two fibers.

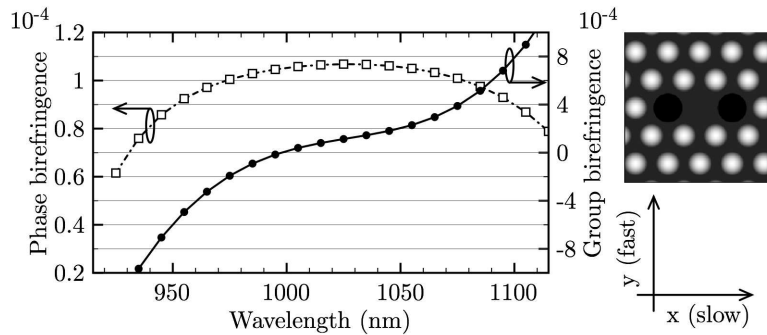


Fig. 8. Calculated group and modal phase birefringence for a fiber with B-doped stress applying parts

Figure 8 and 9 show the calculated modal phase birefringence along with the corresponding group birefringence for fibers similar to fibers I and II, respectively.

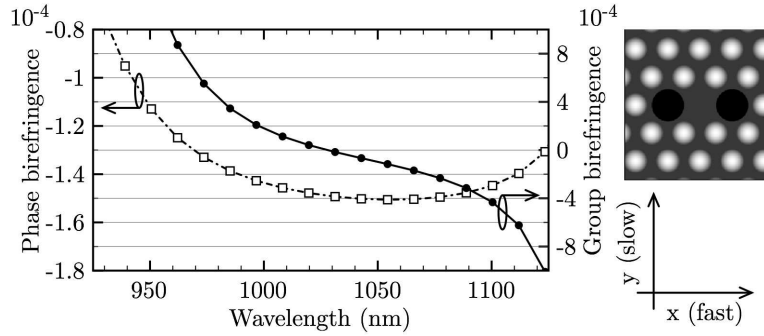


Fig. 9. Calculated group and modal phase birefringence for a fiber with F-doped stress applying parts

There is in general a good agreement between the calculated and the measured modal phase and group birefringence for the two fibers. As was observed experimentally, the fast and slow axes are reversed in the fiber with F-doped inclusions compared to the fiber with B-doped inclusions and a conventional PANDA fiber. Due to the somewhat arbitrarily chosen draw induced enhancement factor of the stress field originating from the F-doped inclusions, the absolute level of the modal phase birefringence in the modeled fiber II is slightly smaller than the experimental result shown in Fig. (4).

6. Conclusions

Stress caused by Ge-doped cladding rods in a solid hybrid TIR/PBG photonic crystal fiber were found to interfere with the stress field caused by stress applying parts near the core. Consequently, the stress field induced by B-doped SAPs is found to be weakened by the presence of the cladding rods. By instead using F-doped SAPs, with a smaller expansion coefficient than pure silica, the total stress field and thus the polarization maintenance is increased. A polarization maintaining fiber with F-doped SAPs and an h-parameter below $3 \cdot 10^{-5} \text{ m}^{-1}$ was demonstrated.